

# The Significant Differences in Solvation Thermodynamics of C1-C3 Oxygenates in Hydrophilic versus Hydrophobic Pores of a Hydrophilic Ti-FAU Zeolite Model†

Xiuting Chen <sup>a, b</sup> and Rachel B. Getman <sup>a, b \*</sup>

\* Corresponding author: [getman.11@osu.edu](mailto:getman.11@osu.edu)

<sup>a</sup> Department of Chemical and Biomolecular Engineering, Clemson University, Clemson, SC 29634, United States.

<sup>b</sup> Current affiliation: William G. Lowrie Department of Chemical and Biomolecular Engineering, The Ohio State University, Columbus, OH 43220, USA

†Supporting Information (SI) is provided.

## Abstract

The rates of catalytic reactions have been observed to be dramatically different in zeolites, depending on if they are hydrophobic or hydrophilic. Hypotheses aimed at explaining this behavior have pointed to various solvent molecule and zeolite properties as having influence on entropy. Herein, the influence of various solvent and adsorbate properties on the solvation energies, entropies, and free energies of eleven C<sub>1</sub>-C<sub>3</sub> oxygenates in hydrophobic and hydrophilic pores within a hydrophilic model of Ti-FAU zeolite are tested. The results indicate significant variation in the calculated solvation thermodynamics depending on the adsorbate type, as well as if it is bound within a hydrophobic or hydrophilic pore. Further, while solvation energies are related to solvent-adsorbate interactions, solvation entropies have multiple contributions, and these differ depending on if the adsorbate is in a hydrophobic or hydrophilic pore. Specifically, solvation

entropies in hydrophobic pores are related to solvent structural properties, whereas solvation entropies in hydrophilic pores are related to adsorbate polarity. The large range of results obtained from two different pores within one zeolite model with minimal unique adsorption sites suggests that solvation behavior in zeolites is complicated and that the phenomena that control observed performance depend on the zeolite, reaction, and solvent.

## 1. Introduction

Liquid phase catalytic processes play a critical role in sustainable chemistries such as biomass conversion and electrocatalysis.<sup>1,2</sup> Solvents have profound effects on the chemistry of these reactions, for example, by influencing the thermodynamics, kinetics, and coverages of interfacial species,<sup>3–5</sup> which in turn can alter catalytic mechanisms.<sup>6–8</sup> The presence of solvent can also control selectivity, for example, by promoting certain reaction pathways while inhibiting others<sup>9–11</sup>. Complicating this, solvent effects in confined spaces are different than in unconfined spaces.<sup>12–14</sup> For example, there are fewer interactions between water molecules in nanosized pores than in unconfined “bulk” water.<sup>15,16</sup> Further, water structures are influenced by pore geometries<sup>17</sup>, and this can influence the free energies of interfacial species<sup>18</sup>. Variations in the size and shape of the pores, as well as different chemical properties of the pore environment can also influence catalytic phenomena.<sup>9,14,19–24</sup>

Zeolites are excellent materials for learning about the roles of solvents in microporous catalysts. Zeolites are microporous crystalline materials primarily comprised of silica tetrahedra.<sup>25–27</sup> Their catalytic activity and selectivity can be tuned via their compositions and/or pore topologies.<sup>28,29</sup> Zeolites can further be made more or less hydrophilic (or hydrophobic) in order to tune performance through solvent effects.<sup>13,30,31</sup> Strategies for tuning zeolite hydrophilicity include

the formation of metal-OH groups by substituting framework Si atoms with lower-valent metal atoms, which results in compensating protons, as well as the hydrolysis of Si-O-Si bridges, which creates silanol groups (Si-OH).<sup>2,31-34</sup> The hydroxyl groups are hydrophilic and hence promote clustering of water molecules.<sup>17,32,35</sup>

Effects of solvents on zeolite catalysis have been investigated with different distributions and ratios of hydroxyl groups to learn the influence of pore hydrophilicity (or hydrophobicity) on reaction kinetics.<sup>36-38</sup> Studies have found that aldol addition<sup>39</sup>, hydrogenation<sup>40</sup>, and glucose isomerization<sup>2,10,41</sup> reactions exhibit higher rates when fewer hydroxyl groups are present (i.e., more hydrophobic zeolites), whereas alkene epoxidation<sup>20,42,43</sup> exhibits higher conversions, rates, and selectivities when more hydroxyl groups are present (i.e., more hydrophilic zeolites). The difference in performance between hydrophobic and hydrophilic zeolites has been suggested to result from differences in water molecule densities within the zeolite pores. For example, the better performance of hydrophilic zeolites for alkene epoxidation has been attributed to large and positive changes in entropies of solvation caused by destruction of water molecule clusters within the pores due to formation of a transition state.<sup>20</sup> Additionally, the better performance of hydrophobic zeolites for glucose isomerization has been attributed to the relatively larger mobilities of the intermediate species within the pores due to less confinement by water molecule clusters compared to in hydrophilic pores.<sup>10</sup> Further, *ab initio* molecular dynamics (AIMD) simulations suggest that the existence of extended hydrogen bonding networks around the reactant species in hydrophilic pores hinders the formation of intermediate species.<sup>44</sup> Clearly, zeolite hydrophilicity influences observed catalytic phenomena. However, solvent effects for any given reaction seem to be reaction specific. To provide insights into these differences, computational studies have investigated solvent structures within zeolite pores and how they influence species free energies.<sup>42,45-48</sup> Density

functional theory (DFT) calculations indicate that water molecule adsorption energies increase (become more negative) as the water density increases.<sup>47</sup> However, the origin of the different ways that solvents influence catalytic performance in zeolites remains unresolved.

Our goal in this work is to provide further insights into the molecular phenomena that control solvent effects in zeolites. Since catalytic performance can be traced to solvation thermodynamics, we specifically evaluate the influences of pore hydrophilicity, solvent molecule structure and mobility, and adsorbate properties on the solvation thermodynamics of species bound in zeolite pores. To do this, we use our previously developed method of multiscale sampling (MSS)<sup>49</sup>, which combines force field molecular dynamics (MD) and DFT. We compute the energies, entropies, and free energies of solvation of eleven C<sub>1</sub>-C<sub>3</sub> oxygenate species in Ti-FAU zeolite in water solvent. To investigate the influence of hydrophilicity, we compute these values in pores with and without hydroxyl groups. In other words, we investigate the influence of *pore* hydrophilicity/hydrophobicity on the solvation thermodynamics of species adsorbed within a hydrophilic zeolite. This is done since a zeolite model without any hydroxyl groups (or other defects) is perfectly hydrophobic, hence preventing solvation in our simulations. Our simulations show that free energies of solvation can be positive or negative, depending on whether the adsorbate is located within a hydrophilic or hydrophobic pore. They further suggest that pore hydrophilicity impacts water molecule mobility, but that there is not an obvious correlation with solvation thermodynamics. Instead, our results suggest that entropy within hydrophilic pores is more related to adsorbate properties, while entropy within hydrophobic pores is more related to solvent structure.

## 2. Methodology

### 2.1 Model building

FAU is chosen as a model because it comprises only one symmetrically unique tetrahedral site. It hence allows us to focus on the influence of hydrophilicity rather than various possible adsorption sites. The structure of FAU is obtained from the International Zeolite Association Database<sup>50</sup>, and a  $1 \times 1 \times 2$  supercell is cleaved from that structure<sup>54</sup>. The active site is constructed by replacing one tetrahedral Si atom with a Ti atom (Figure 1a). The cell parameters are then relaxed in DFT, which yields final optimized values of  $x = y = 24.433 \text{ \AA}$ ,  $z = 48.866 \text{ \AA}$ , and  $\alpha = \beta = \gamma = 90^\circ$ . Hydroxyl groups are incorporated by removing another Si atom and saturating the four broken bonds with H atoms. In hydrophilic pore models, the Si atom that is coordinated to the Ti atom is removed (Figure 1b) whereas in hydrophobic pores, a Si atom at least  $7 \text{ \AA}$  away from the Ti atom is removed. Adsorbates are bonded to the Ti sites in both models. To obtain adsorbate geometries, the adsorbate structure, Ti atom, O atoms coordinated to the Ti atom, and the hydroxyl groups in the hydrophilic pore are relaxed in DFT. We refer to this group of atoms as the “relaxed region” in the remainder of this manuscript. A flow diagram of this procedure is provided in Figure S3.

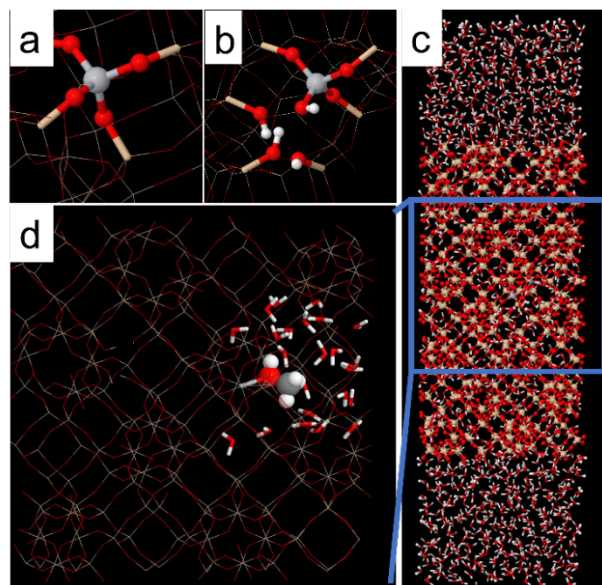


**Figure 1.** a) Adsorbate binding site in the hydrophobic pore model. b) Adsorbate binding site in the hydrophilic pore model. c) Zeolite model used in molecular dynamics simulations. d) Truncated zeolite model used in density functional theory calculations. Ti = silver, O = red, Si = beige, C = gray, H = white. Atoms shown in ball and stick representation versus wireframe are for visual clarity.

Water is introduced to the zeolite as follows. A water column is created in a separate supercell by adding 1200 H<sub>2</sub>O molecules to a simulation box with dimensions  $x = y = 24.433 \text{ \AA}$ ,  $z = 110 \text{ \AA}$ , and  $\alpha = \beta = \gamma = 90^\circ$  using the MCPlIQ code.<sup>49</sup> The density of H<sub>2</sub>O in this box is equilibrated in MD in the isothermal isobaric (NPT) ensemble at 300 K and 1 atm, which results in a height of  $z = 68.134 \text{ \AA}$ . The zeolite is then cleaved in the  $z$  direction, and  $70 \text{ \AA}$  vacuum space is added between periodic images. The water column is then inserted into this space. In cleaving the zeolite, the cut is made such that the Ti site is at least  $12 \text{ \AA}$  from the zeolite/water interface. This is done to avoid interfacial effects at the Ti site (see Supporting Information S1.2 for more details). Following incorporation into the zeolite supercell, the density of water in the middle of the water column is re-equilibrated in the NPT ensemble. During this simulation, water molecules from the water column are pushed into the zeolite (Figure 1c), resulting in a decrease in the supercell height.

Final values of  $z$  range between 86 Å and 88 Å (Figure S4), depending on the adsorbate. Configurations of H<sub>2</sub>O molecules are generated in MD using this model. However, this model comprises 1200 H<sub>2</sub>O molecules, which is computationally intractable for DFT. Hence, this supercell is truncated into a 1×1×1 supercell and most of the H<sub>2</sub>O molecules are removed (Figure 1d) prior to DFT calculations. Specifically, all H<sub>2</sub>O molecules with center of mass farther than 7 Å from the center of mass of the adsorbate are removed, leaving ~ 20-25 H<sub>2</sub>O molecules, depending on the adsorbate. Further details about the DFT model are provided in Supporting Information Section S1.5.

## 2.2 Adsorbates

Eleven C<sub>1</sub>-C<sub>3</sub> alcohol, aldehyde, and polyol species are considered in this study. These are chosen to study the influence of -OH functional groups (or lack thereof) on solvation thermodynamics, since our prior work indicates that -OH groups can induce significant solvation effects<sup>51</sup>. Further, we consider adsorbates with stoichiometry ranging from C<sub>1</sub>-C<sub>3</sub> in order to learn the influence of adsorbate size (modeled using solvent accessible surface area, or SASA; see below) on solvation thermodynamics in confined systems. Conformations of adsorbates used in this work are depicted in Figure 2 for the hydrophilic pore and in Figure S6 for the hydrophobic pore. In general, we find that species bind to Ti via their oxygen atoms. As polyol species comprise multiple oxygen atoms, we include multiple conformers for each polyol. Further, since the -OH groups of polyols can interact with the hydroxyl groups in hydrophilic pores, additional conformations with different degrees of interaction with the pore are also included. However, we do not endeavor to identify all possible conformations of each adsorbate in this work to maintain computational tractability and instead focus on understanding how pore hydrophilicity, solvent structure and mobility, and adsorbate properties influence solvation thermodynamics. In total, we consider two conformations

of ethylene glycol (Figures 2h and 2i and S6h and S6i), three conformations of propylene glycol (Figures 2j-2l and S6j-S6l) and glycerol (Figures 2q-2s and S6q-S6s), and four conformations of 1,3-propanediol (Figures 2m-2p and S6m-S6p) within each pore.

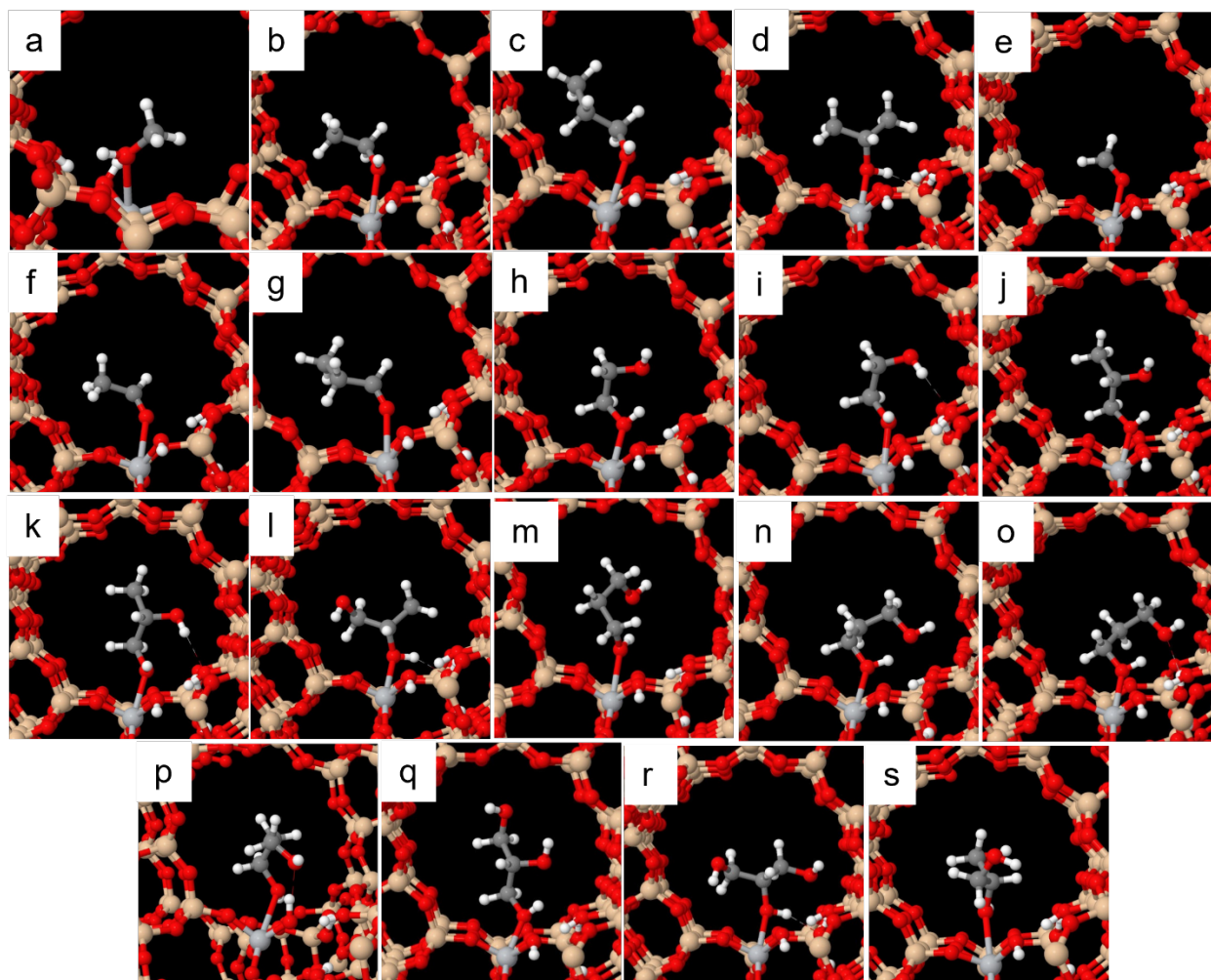


**Figure 2.** Adsorbate structures in the hydrophilic pore model. a) Methanol, b) Ethanol, c) Propanol, d) Isopropanol, e) Formaldehyde, f) Acetaldehyde, g) Propionaldehyde, h) Ethylene Glycol (Geometry 1), i) Ethylene Glycol (Geometry 2), j) Propylene Glycol (Geometry 1), k) Propylene Glycol (Geometry 2), l) Propylene Glycol (Geometry 3), m) 1,3-Propanediol (Geometry 1), n) 1,3-Propanediol (Geometry 2), o) 1,3-Propanediol (Geometry 3), p) 1,3-Propanediol (Geometry 4), q) Glycerol (Geometry 1), r) Glycerol (Geometry 2), s) Glycerol (Geometry 3). Ti = silver, O = red, Si = beige, C = gray, H = white.

## 2.3 Free Energies

Free energies of solvation are calculated using the method of MSS similar to our prior work:<sup>52,53</sup>

$$\Delta F^{MSS} = \Delta E^{DFT} - T\Delta S^{MD} \quad (1)$$

where  $\Delta F^{MSS}$  is Helmholtz free energy of solvation,  $\Delta E^{DFT}$  is the water-adsorbate interaction energy calculated with DFT,  $T$  is temperature, and  $\Delta S^{MD}$  is the water-adsorbate interaction entropy calculated with MD.  $\Delta E^{DFT}$  is an average over ten configurations of H<sub>2</sub>O molecules (generated in MD; see Section 2.3.1):

$$\Delta E^{DFT} = \langle (E_{ads+zeo}^{aq} - E_{ads+zeo}^g) - (E_{zeo}^{aq} - E_{zeo}^g) \rangle \quad (2)$$

where  $E_{ads+zeo}^{aq}$  is the electronic energy of the zeolite with the adsorbate in water,  $E_{ads+zeo}^g$  is electronic energy of the zeolite with adsorbate (no water molecules),  $E_{zeo}^{aq}$  electronic energy of the zeolite and water molecules (no adsorbate), and  $E_{zeo}^g$  is electronic energy of the zeolite (no adsorbate or water molecules). Details about how these are obtained are provided in Section 2.3.2.

The water-adsorbate interaction entropy is calculated by equation (3)

$$T\Delta S^{MD} = \Delta E^{MD} - \Delta F^{MD} \quad (3)$$

where  $\Delta E^{MD}$  is the average energy of interaction calculated between the water molecules and the adsorbate in MD and  $\Delta F^{MD}$  is Helmholtz free energy of solvation calculated using the method of thermodynamic integration in MD (see Section 2.3.1). Free energies of adsorption are calculated by adding the free energy of solvation to the gas phase adsorption energy:

$$\Delta F_{ads}^{aq} = \Delta E_{ads}^g + \Delta F^{MSS} \quad (4)$$

$\Delta E_{ads}^g = E_{C_xH_yO_z^*}^g - E_{C_xH_yO_z}^g - E_*^g$ , where  $E_{C_xH_yO_z^*}^g$ ,  $E_{C_xH_yO_z}^g$ , and  $E_*^g$  are the electronic energies of the adsorbed structure, isolated molecule, and “clean” (i.e., adsorbate-free) zeolite in vacuum.

### 2.3.1 MD simulations

MD simulations are performed using the Large-scale Atomic/Molecular Massively Parallel Simulator (LAMMPS) software<sup>54</sup> on the system illustrated in Figure 1c. In all MD simulations, the zeolite and adsorbate atoms are held fixed, and the H<sub>2</sub>O molecules are moved according to Newton’s equations of motion. All MD simulations utilize a time step of 1 fs, and all begin with an energy minimization until the energy is converged to within 10<sup>-8</sup> eV. Following addition of the adsorbate, a simulation in the NPT ensemble is carried out at 300 K and 1 atm for 10 ns, where the pressure and temperature are maintained by the Nosé-Hoover thermostat and barostat. Following this step, the density of water 10-20 Å from the zeolite surface is 1.02~1.05 g/cm<sup>3</sup> (Figure S2), which is comparable to the bulk density of the water force field<sup>55</sup>. Next, simulations in the canonical (NVT) ensemble are performed at 300 K for 10 ns to equilibrate H<sub>2</sub>O molecule configurations. Production runs of 5 ns are then carried out and sampled as follows. Configurations used to compute  $\Delta E^{DFT}$  are sampled every 0.5 ns and  $\Delta E^{DFT}$  is computed via Equation 2. Configurations used to compute  $\Delta E^{MD}$  are sampled every 0.001 ns and  $\Delta E^{MD}$  is computed as the average water-adsorbate interaction energy. Configurations used to compute the number of adsorbate-H<sub>2</sub>O hydrogen bonds and H<sub>2</sub>O-H<sub>2</sub>O hydrogen bonds are sampled every 0.05 ns and hydrogen bonds are counted according to the geometric criteria that the distance between the oxygen atom on the hydrogen bond acceptor and the oxygen atom on the hydrogen bond donor is less than 3.5 Å and that the hydrogen bond acceptor oxygen-hydrogen-hydrogen bond donor oxygen angle is between 150° and 180°. Configurations used to compute the numbers of water

molecules in the pores are sampled every 0.05 ns and counted as those water molecules with center of mass within 10 Å of the framework Ti atom. Configurations used to compute the total dipole-dipole time correlation function (TCF) are sampled every 100 fs and the ensemble average is calculated as<sup>56,57</sup>

$$C(t) = \frac{\langle \vec{M}(t+t_0) \cdot \vec{M}(t_0) \rangle}{\langle |\vec{M}(t_0)|^2 \rangle} \quad (5)$$

where  $\vec{M} = \sum_i \mu_i$  and  $\mu_i$  are dipole moment vectors summed over the  $i$  H<sub>2</sub>O molecules with center of mass within 10 Å of the framework Ti atom.  $\vec{M}(t+t_0)$  and  $\vec{M}(t_0)$  are the total dipole moments at time  $t$  and initial time  $t_0$ , respectively. In this notation, a new interval is started every 0.1 ps, and  $t$  is the time elapsed since  $t_0$ , taken in 0.1 ps intervals up to a total interval time of 12 ps.

### 2.3.1.1 Force field and partial charge of atoms

Pairwise interaction energies are computed using Lennard-Jones + Coulomb (LJ+C) potentials. LJ interactions are computed to a cutoff of 7 Å. The TIP3P/CHARMM model<sup>58</sup> is used for H<sub>2</sub>O molecules, which are held rigid using the SHAKE algorithm. LJ parameters for adsorbate and zeolite atoms are constructed as follows. The TraPPE-Zeo force field<sup>59</sup> is used for framework Si atoms and O atoms, with the exceptions of the O atom coordinated to the Ti atom and the O atoms in the hydroxyl groups. The O and H atoms in the hydroxyl groups employ parameters from the OPLS-AA<sup>60</sup> force field for alcohols. The O atom coordinated to the Ti atom and the Ti atom employ a LJ potential created by Matsui and Akaogi for a TiO<sub>2</sub> slab.<sup>61,62</sup> We specifically use the parameters converted into a LJ potential by Lyubartsev et al.<sup>61</sup> Justification of this choice is provided in Supporting Information Section S1.6. LJ parameters for adsorbates are modeled with

the OPLS-AA<sup>60</sup> force field. Parameters for all atom types are listed in Supporting Information Section S1.7. Lorentz-Berthelot mixing rules are used to compute cross-terms between the zeolite and water molecules, and geometric mixing rules are employed to compute cross-terms between adsorbates and water molecules. Long-range Coulombic interactions are calculated with the particle-particle particle-mesh (PPPM) method. To take into account charge transfer between the adsorbate and zeolite, the DFT-calculated partial charges are used as the Coulomb charges on adsorbate and zeolite atoms. We find that charge transfer is small in all cases (maximum charge transfer to any adsorbate is  $|0.14| h^+$ ) and that most of the transferred charge resides within the relaxed region. We hence restrict all the charge transfer to the relaxed region by evenly distributing the partial charge of the adsorbate over the atoms in this region, leaving the partial charges on the framework Si atoms and all other O atoms fixed at the values calculated in the absence of the adsorbate. An example of this procedure is provided in Supporting Information Section S1.8.

### 2.3.1.2 Helmholtz free energy of solvation

Helmholtz free energy of solvation calculations are performed in the NVT ensemble using the finite-difference thermodynamic integration (FDTI) method of Mezei<sup>63</sup>. In these calculations, the LJ interactions between all water molecules and the adsorbate and Coulomb interactions between all water molecules and the adsorbate and the relaxed region of the zeolite model are “scaled” with scaling parameter  $\lambda$  in 51 equally spaced steps. For each value of  $\lambda$ , an NVT simulation is carried out for 300 ps, where the first 50 ps is used to equilibrate the system. A free energy difference of each step is then calculated using a perturbation method over  $\lambda$  to obtain the free energy of solvation. A soft-core potential is used to avoid a singularity when  $\lambda=0$ .<sup>64</sup> To isolate the contribution due to the water-adsorbate interaction, the free energy of the clean zeolite is subtracted out:

$$\Delta F^{MD} = \Delta F_{ads+zeo}^{MD} - \Delta F_{zeo}^{MD} \quad (6)$$

where  $\Delta F_{ads+zeo}^{MD}$  includes scaling of the LJ and Coulomb potentials, and  $\Delta F_{zeo}^{MD}$  involves scaling only of the Coulomb potential.

### 2.3.2 DFT calculations

Periodic DFT simulations are carried out with the CP2K program<sup>65</sup> using the Perdew–Burke–Ernzerhof (PBE) form of the generalized gradient approximation (GGA), DZVP-MOLOPT-SR-GTH basis set for valence electrons, and Goedecker-Teter-Hutter (GTH) pseudopotentials for core electrons. Plane waves are included to a cutoff energy of 360 Ry. Grimme’s D3 dispersion corrections with Becke–Johnson damping<sup>66</sup> are employed. Electronic energies are calculated self-consistently at the  $\Gamma$ -point and are considered to be converged when the difference in energy between subsequent steps falls below  $10^{-6}$  Ha. Atomic partial charges are derived from the calculated electronic structures using the DDEC6 program<sup>67</sup>. Geometry relaxations are carried out until the maximum force and root-mean-square displacement fall below  $5 \times 10^{-5}$  Bohr/Ha and 0.0005 Bohr, respectively. Geometry relaxations are carried out as follows. To obtain the structure for the Ti-substituted zeolite, all atom coordinates and cell vectors are relaxed, while the cell angles are held fixed. Following addition of the adsorbate, the adsorbate and atoms in the relaxed region are relaxed, while all remaining atoms as well as the cell vectors and angles are held fixed. To compute  $\Delta E^{DFT}$ , adsorbate atoms are allowed to relax when calculating  $E_{ads+zeo}^{aq}$ , while all other atoms and the zeolite framework are held fixed. To compute the remaining terms in  $\Delta E^{DFT}$ , all atoms are held fixed with positions adopted from the  $E_{ads+zeo}^{aq}$  calculation.

## 2.4 Adsorbates dipole moments

Adsorbate dipole moments are computed from the atomic positions and partial charges calculated in DFT using the standard equation for dipole moment, i.e.,  $\mu = \sum_i q_i \cdot r_i$ , where  $i$  is over atoms,  $q$  are DFT calculated partial charges, and  $r$  are the x, y, z coordinates of the nuclei. Because adsorbates have non-zero partial charges, dipole moments depend on the coordinate system. The adsorbate center of mass of is used as the reference origin.

## 2.5 Solvent Accessible Surface Area (SASA)

We find that adsorbate solvent accessible surface areas (SASAs) are loosely correlated to solvation thermodynamics. We calculate these values using the PyMOL package.<sup>68</sup> Specifically, a sphere with a radius of 1.4 Å (equal to the kinetic diameter of a H<sub>2</sub>O molecule) is “rolled” over the zeolite surface and the SASA is computed. Simulations are performed with and without the adsorbate and subtracted to estimate the adsorbate surface area that is accessible to a H<sub>2</sub>O molecule.

# 3. Results

## 3.1 Free energies of adsorption

Calculated values of  $\Delta F_{ads}^{aq}$  are tabulated in Table 1. For each adsorbate type,  $\Delta F_{ads}^{aq}$  for the conformation that minimizes  $\Delta F_{ads}^{aq}$  is plotted in Figure 3a. We note that the conformation with the lowest  $\Delta F_{ads}^{aq}$  can differ depending on whether the pore is hydrophilic or hydrophobic. In general, values of  $\Delta F_{ads}^{aq}$  span from  $-0.27$  eV to  $-0.96$  eV in the hydrophilic pore and from  $-0.39$  eV to  $-0.87$  eV in the hydrophobic pore. These values are within the range of values reported in the literature.<sup>69–72</sup> In general,  $\Delta F_{ads}^{aq}$  for alcohols and aldehydes are more negative in the hydrophobic

pore, while  $\Delta F_{ads}^{aq}$  for polyols are more negative in the hydrophilic pore; however, there is only slight distinction between  $\Delta F_{ads}^{aq}$  for C<sub>3</sub> polyols.

Table 1: Calculated free energies of adsorption, free energies of solvation, energies of solvation, and entropies of solvation multiplied by temperature for the conformers studied in this work in the hydrophilic and hydrophobic pore models in units of eV at 300 K.

Name	Hydrophilic Pore				Hydrophobic Pore			
	$\Delta F_{ads}^{aq}$	$\Delta F^{MSS}$	$\Delta E^{DFT}$	$T\Delta S^{MD}$	$\Delta F_{ads}^{aq}$	$\Delta F^{MSS}$	$\Delta E^{DFT}$	$T\Delta S^{MD}$
Methanol	-0.36*	0.14	-0.22	-0.37	-0.72*	-0.19	-0.52	-0.34
Ethanol	-0.55*	0.17	-0.29	-0.46	-0.87*	-0.25	-0.58	-0.33
Propanol	-0.67*	0.18	-0.36	-0.54	-0.84*	-0.17	-0.59	-0.43
Isopropanol	-0.69*	0.12	-0.28	-0.40	-0.71*	-0.08	-0.54	-0.46
Formaldehyde	-0.27*	0.27	-0.31	-0.58	-0.39*	-0.02	-0.32	-0.30
Acetaldehyde	-0.43*	0.21	-0.47	-0.68	-0.63*	-0.15	-0.52	-0.36
Propionaldehyde	-0.42*	0.31	-0.40	-0.71	-0.67*	-0.07	-0.50	-0.42
Ethylene Glycol (Geometry 1)	-0.73*	0.02	-0.73	-0.76	-0.51*	-0.05	-0.67	-0.62
Ethylene Glycol (Geometry 2)	-0.29	0.13	-0.54	-0.66	-0.49	-0.19	-0.88	-0.69
Propylene Glycol (Geometry 1)	-0.88*	-0.04	-0.87	-0.84	-0.66	-0.06	-0.76	-0.70
Propylene Glycol (Geometry 2)	-0.39	0.08	-0.69	-0.77	-0.44	-0.12	-0.85	-0.73
Propylene Glycol (Geometry 3)	-0.87	-0.15	-0.55	-0.40	-0.81*	-0.36	-0.95	-0.59
1,3-Propanediol (Geometry 1)	-0.62	0.10	-0.64	-0.74	-0.80*	-0.16	-0.55	-0.40
1,3-Propanediol (Geometry 2)	-0.77	0.11	-0.75	-0.86	-0.68	-0.02	-0.73	-0.70
1,3-Propanediol (Geometry 3)	-0.83*	0.10	-0.72	-0.83	-0.63	-0.06	-0.65	-0.59
1,3-Propanediol (Geometry 4)	-0.61	0.15	-0.83	-0.97	-0.69	-0.04	-0.70	-0.66
Glycerol (Geometry 1)	-0.69	0.09	-0.96	-1.05	-0.70	-0.26	-1.10	-0.84
Glycerol (Geometry 2)	-0.96*	-0.21	-0.87	-0.66	-0.86*	-0.38	-0.95	-0.57
Glycerol (Geometry 3)	-0.68	-0.14	-0.83	-0.69	-0.75	-0.30	-0.97	-0.67

\*Conformer with the lowest value of  $\Delta F_{ads}^{aq}$ .

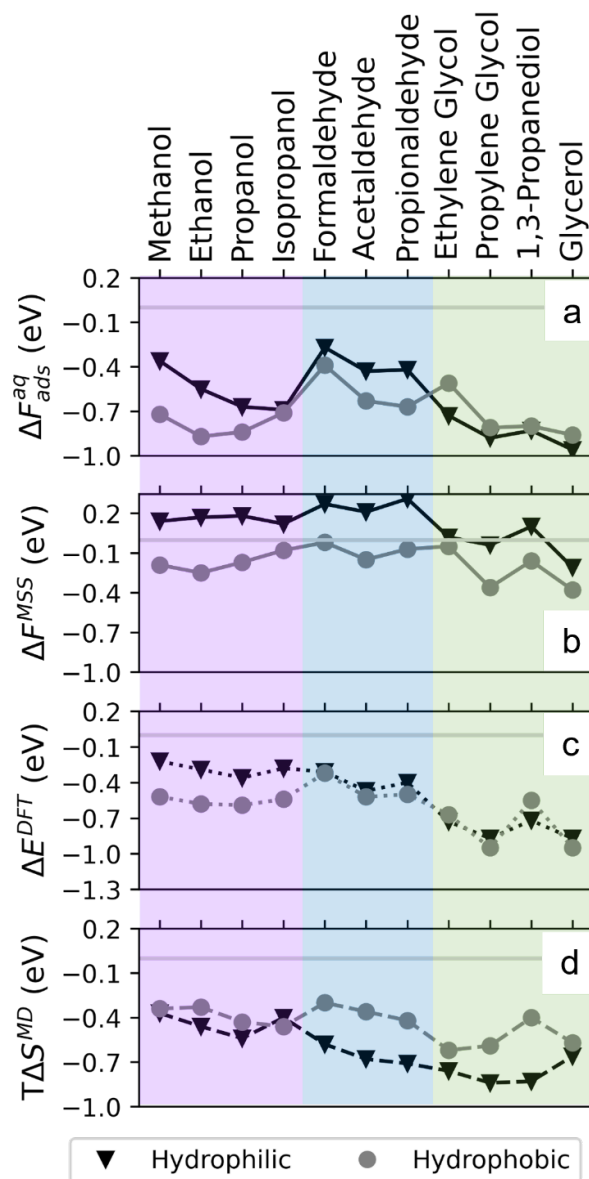


**Figure 3.** Free energies of adsorption (a), free energies of solvation (b), energies of solvation (c), and entropies of solvation multiplied by temperature (d) for the conformers with the lowest free energies of adsorption (i.e., the \*'ed species in Table 1) in the hydrophilic (black triangles) and hydrophobic (gray circles) pore models. Lines connecting the data points are for visual purposes only.

### 3.2 Free energies of solvation

Values of  $\Delta F^{MSS}$  are tabulated in Table 1 and plotted for the conformation that minimizes  $\Delta F_{ads}^{aq}$  in Figure 3b.  $\Delta F^{MSS}$  span from  $-0.02$  eV to  $-0.38$  eV and are in general less than 0 in the hydrophobic pore. In the hydrophilic pore,  $\Delta F^{MSS}$  span from  $-0.21$  eV to  $+0.31$  eV. In contrast to the hydrophobic pore,  $\Delta F^{MSS}$  in the hydrophilic pore are positive, except for propylene glycol and glycerol. These results indicate that  $\Delta F^{MSS}$  stabilizes species in the hydrophobic pore but destabilizes species in the hydrophilic pore. These results are in agreement with our prior work which compared  $\Delta F^{MSS}$  for species adsorbed to hydrophobic (Pt(111), negative  $\Delta F^{MSS}$ ) and hydrophilic (Pt/Al<sub>2</sub>O<sub>3</sub>, positive  $\Delta F^{MSS}$ ) slabs.<sup>51</sup>

Differences in species stabilization has been hypothesized to account for differences in activity observed in hydrophilic versus hydrophobic *zeolites*. While we have not specifically examined hydrophobic zeolites, we can provide some insights into such systems. Specifically, in a perfectly hydrophobic zeolite, there would be no free energy of solvation. Hence, a distinction between a perfectly hydrophobic zeolite and a hydrophilic zeolite such as the one studied in this work can be made by considering the free energy of solvation. We find that  $\Delta F^{MSS}$  are positive in the hydrophilic pore and negative in the hydrophobic pore. Water hence stabilizes species in the hydrophobic pore and destabilizes species in the hydrophilic pore.

### 3.3 Energies and entropies of solvation

$\Delta E^{DFT}$  and  $T\Delta S^{MD}$  are tabulated in Table 1 and plotted for the conformation that minimizes  $\Delta F_{ads}^{aq}$  in Figures 3c and 3d, respectively.  $\Delta E^{DFT}$  span from  $-0.22$  eV to  $-0.95$  eV and are for the most part similar in hydrophobic and hydrophilic pores, with the exception of monoalcohol species, where  $\Delta E^{DFT}$  are more negative in the hydrophobic pore.  $T\Delta S^{MD}$  span from  $-0.37$  eV to  $-0.84$  eV

in the hydrophilic pore and from  $-0.30$  eV to  $-0.62$  eV in the hydrophobic pore. In contrast to  $\Delta E^{DFT}$ , values of  $T\Delta S^{MD}$  are similar for monoalcohols in hydrophobic and hydrophilic pores, while for aldehydes and polyols,  $T\Delta S^{MD}$  are more negative in the hydrophilic pore. The difference in  $\Delta F^{MSS}$  observed between hydrophobic and hydrophilic pores is hence due to  $\Delta E^{DFT}$  for monoalcohols and  $T\Delta S^{MD}$  for aldehydes and polyols.

Differences in energies and entropies of solvation between hydrophilic and hydrophobic zeolites have been shown to result in differences in catalytic performance. Further, these differences have been suggested to result from various molecular level phenomena, including differences in solvent molecule density and displacement and solvent molecule and species mobilities. Using our calculated values for  $\Delta E^{DFT}$  and  $T\Delta S^{MD}$ , we have interrogated several of these phenomena plus others and their relationship to  $\Delta E^{DFT}$  and  $T\Delta S^{MD}$ . Unsurprisingly, we find that  $\Delta E^{DFT}$  is related to solvent-species interactions. These results are discussed in Supporting Information Figure S14. We find that  $T\Delta S^{MD}$  has more complex origins which are discussed below.

### 3.4 Entropy relationship to adsorbate and solvent properties

#### 3.4.1 Water density

Density of  $\text{H}_2\text{O}$  molecules in zeolite pores has been suggested to influence catalytic activity in hydrophilic zeolites through various effects caused by the creation and destruction of water molecule clusters.<sup>10,20</sup> To probe the relationship between water molecule density and solvation entropy, we calculate the average number of water molecules in our hydrophilic and hydrophobic pore models (Figure 4a). Specifically, Figure 4a shows the number of  $\text{H}_2\text{O}$  molecules in the hydrophilic (black) and hydrophobic (gray) pore with and without an adsorbate. We specifically use 1,3-propanediol and isopropanol as illustrative adsorbates, since 1,3-propanediol exhibits the

same  $\Delta E^{DFT}$  but different  $T\Delta S^{MD}$  in the hydrophilic vs hydrophobic pore, whereas isopropanol exhibits different  $\Delta E^{DFT}$  but the same  $T\Delta S^{MD}$ .

Figure 4a tells us two things. First, when no adsorbate is present, the numbers of water molecules in the hydrophobic and hydrophilic pores are equal, illustrated by the solid black and gray bars. We also find equal numbers of H<sub>2</sub>O-H<sub>2</sub>O hydrogen bonds when no adsorbate is present (Figure 4b), suggesting that the sizes of water molecule clusters in the absence of an adsorbate are similar regardless of the pore model. Hence, in our hydrophilic zeolite model, H<sub>2</sub>O molecule densities and the sizes of H<sub>2</sub>O molecule clusters do not depend on whether the *pore* is hydrophobic or hydrophilic. Second, when adsorbates are introduced, the number of water molecules in each type of pore indeed decreases, and the amount by which this number decreases is indeed larger in the hydrophilic pore (however, the change in the number of water molecules is similar to the standard deviations, which are caused by fluctuations in the water structures). For example, the number of water molecules decreases by 4.3 and 3.2 when 1,3-propanediol is introduced into the hydrophilic and hydrophobic pore, respectively, and by 4.7 and 3.6 when isopropanol is introduced into the hydrophilic and hydrophobic pore, respectively. Interestingly, the changes in the numbers of water molecules are the same for 1,3-propanediol and isopropanol. In contrast, these two adsorbates exhibit opposite trends in  $\Delta E^{DFT}$  and  $T\Delta S^{MD}$ . While these results cannot be used to rationalize differences in behavior between hydrophilic and hydrophobic *zeolites* (since we have not studied a hydrophobic zeolite), they do suggest that solvation thermodynamics have origins other than H<sub>2</sub>O molecule density and cluster size.

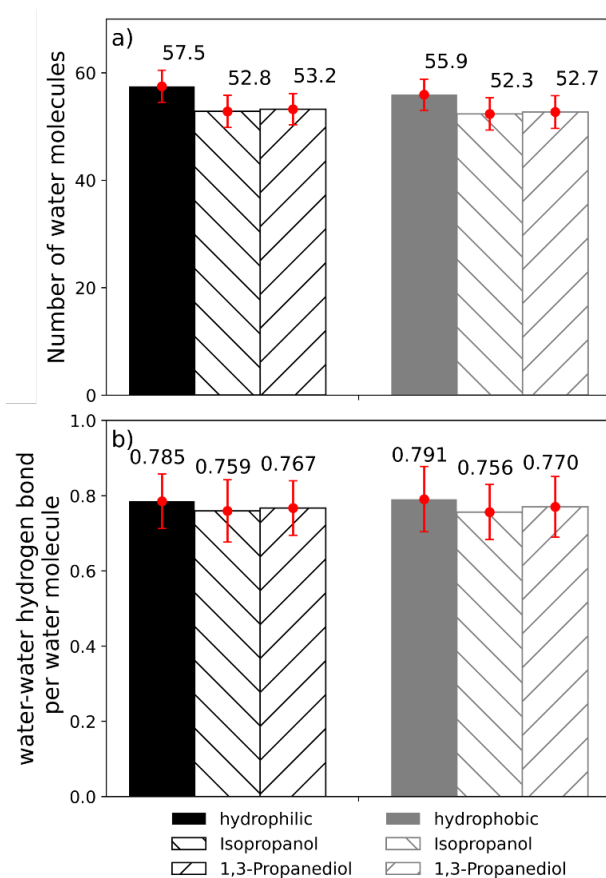


**Figure 4.** Number of water molecules (a) and number of H<sub>2</sub>O-H<sub>2</sub>O hydrogen bonds (b) in the hydrophilic (black) and hydrophobic (gray) pore models in the absence (solid fill) and presence (hashed fill) of isopropanol (forward hashes) and 1,3-propanediol (backward hashes). Error bars (red) are the standard deviations.

### 3.4.2 Water molecule mobilities

Another possibility is that solvation thermodynamics are related to H<sub>2</sub>O molecule mobilities.<sup>10,34</sup> Specifically, H<sub>2</sub>O molecules that are liberated from hydrophilic zeolites when an adsorbate is present are hypothesized to have greater mobilities, which is hypothesized to give rise to an entropic effect.<sup>10</sup> To investigate this, TCFs are plotted in Figure 5. In a TCF plot, values closer to 1 indicate more restricted relaxation (here, of the dipole moments of the water molecules around the adsorbates)<sup>73</sup> and hence lower mobilities. Adsorbates in Figure 5 are grouped by type and their TCFs are compared with the clean zeolite pores, represented by the bold gray and bold black lines

in Figures 5a and 5b, respectively. From Figure 5, H<sub>2</sub>O molecule mobilities exhibit varying behaviors. In the hydrophobic pore model, all adsorbates except for 1,3-propanediol and isopropanol restrict H<sub>2</sub>O molecule mobilities with respect to the adsorbate-free analog (Figure 5a). In contrast, H<sub>2</sub>O molecules in the hydrophilic pore model can exhibit lower, similar or higher mobilities in the presence of adsorbate than in the adsorbate-free analog. While H<sub>2</sub>O molecules in the presence of alcohols and polyols can exhibit higher or lower mobilities, H<sub>2</sub>O molecules in the presence of aldehyde adsorbates exhibit similar or higher mobilities. The higher mobilities when adsorbates are present supports the hypothesis that the presence of adsorbates increases H<sub>2</sub>O molecule mobilities in hydrophilic pores, which was hypothesized to be the reason for the larger activity observed in hydrophilic zeolites for alkene epoxidation.

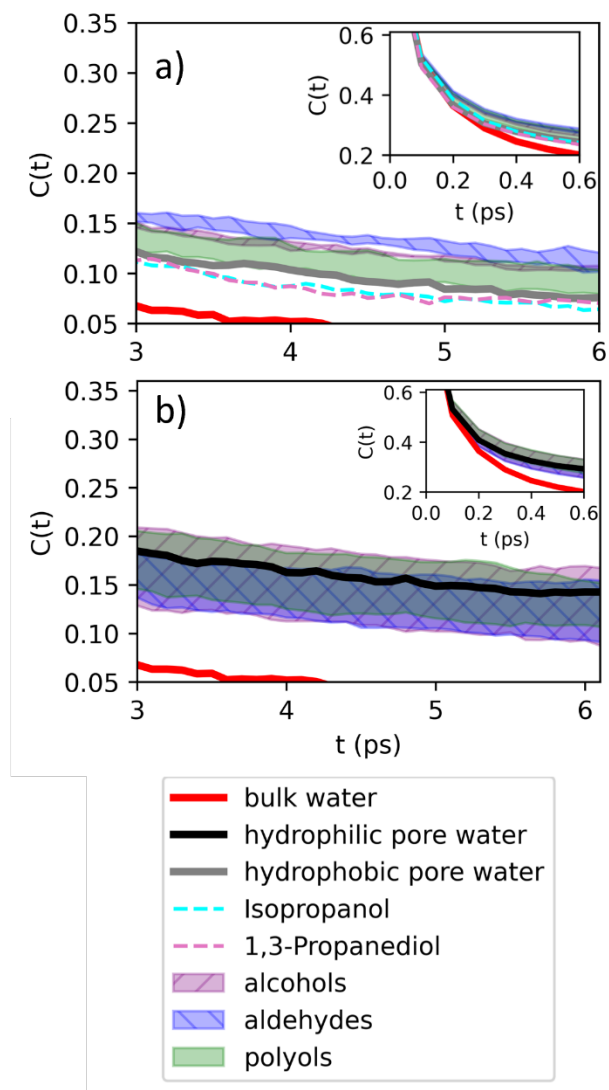


**Figure 5.** Calculated time correlation function illustrating the orientational mobilities of the water molecules in the hydrophobic (a) and hydrophilic (b) pore models in the presences and absence of adsorbates. The solid red lines indicate values for bulk liquid water for comparison.

To investigate if correlation exists between H<sub>2</sub>O molecule mobility and adsorbate entropy, we decomposed the TCFs in Figure 5 into relaxation times by fitting to bi-exponential functions (see Supporting Information Section S2.11).<sup>74</sup> Specifically, we determined the short- and long-time relaxation times for the H<sub>2</sub>O molecules that solvate all adsorbates in both the hydrophilic and hydrophobic pores and then attempted to correlate these values to  $T\Delta S^{MD}$  (see Supporting

Information Figures S10). We find no correlation between either the short- or long-time relaxation times and  $T\Delta S^{MD}$ . We also find no correlation between  $T\Delta S^{MD}$  and the value of TCF (see Supporting Information Table S6). While this does not rule out solvent molecule mobility as a contribution to observed catalytic behavior, it does suggest that solvation entropy has contributions from other phenomena.

### 3.4.3 H<sub>2</sub>O molecule displacement

Another suggestion is that breaking up of H<sub>2</sub>O molecule clusters increases entropy. To investigate this, we calculated the number of H<sub>2</sub>O molecules that are displaced by an adsorbate and plotted this value against  $T\Delta S^{MD}$  in Figure 6a. These correlations give R<sup>2</sup> values of 0.4 and 0.2 for the hydrophobic and hydrophilic pore, respectively, suggesting weak at best correlation. Further,  $T\Delta S^{MD}$  decreases (becomes more negative) as the number of displaced H<sub>2</sub>O molecules increases, which is the opposite of what would be expected if breaking up H<sub>2</sub>O molecule clusters led to an increase in entropy.

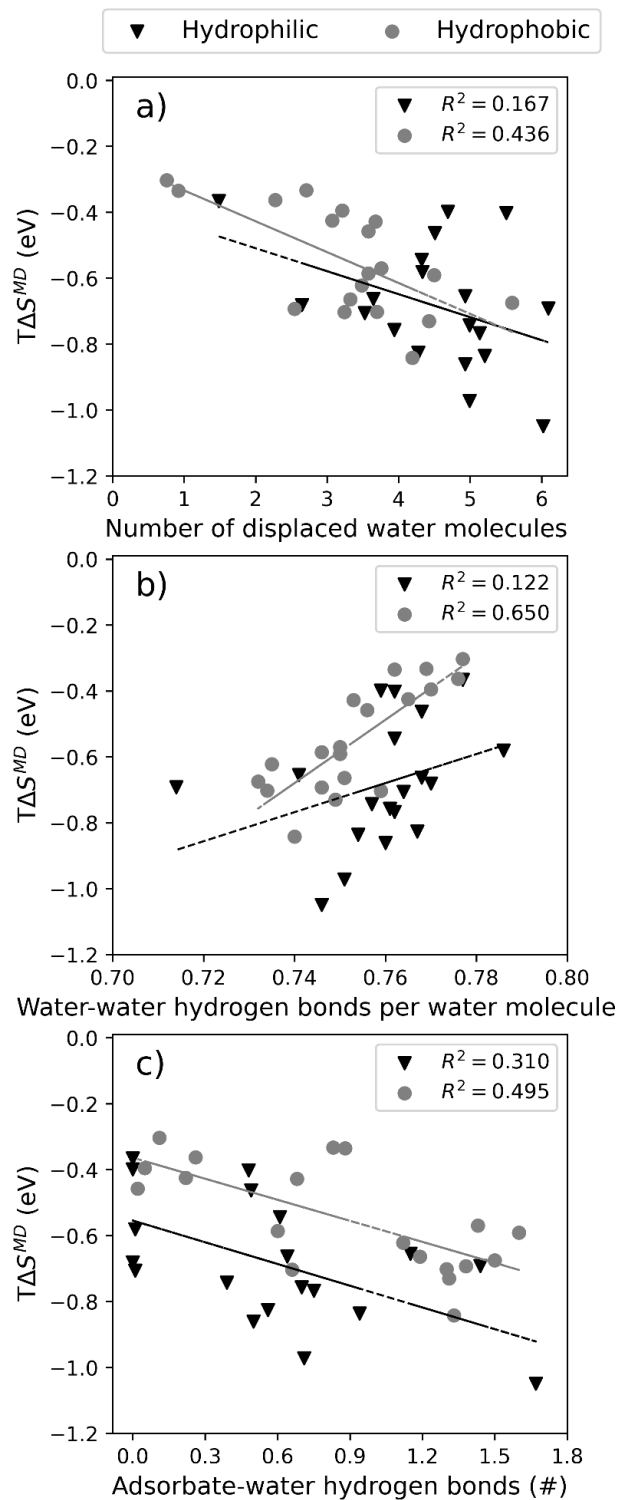


**Figure 6.** Temperature times entropy of solvation versus number of displaced water molecules (a), the number of H<sub>2</sub>O-H<sub>2</sub>O hydrogen bonds (b), and the number of adsorbate-H<sub>2</sub>O hydrogen bonds (c) for the hydrophilic (black triangles) and hydrophobic (gray circles) models. Lines are the least squares best fit lines and  $R^2$  values are the correlation coefficients. T = 300 K.

Another possibility is that disruptions to the H<sub>2</sub>O molecule hydrogen bonding network due to introduction of adsorbates influences H<sub>2</sub>O structural disorder and hence increases entropy. To investigate this,  $T\Delta S^{MD}$  versus the number of H<sub>2</sub>O-H<sub>2</sub>O hydrogen bonds is plotted in Figure 6b. For comparison,  $T\Delta S^{MD}$  versus the number of adsorbate-H<sub>2</sub>O hydrogen bonds is plotted in Figure 6c. R<sup>2</sup> values for  $T\Delta S^{MD}$  versus the number of H<sub>2</sub>O-H<sub>2</sub>O hydrogen bonds and adsorbate-H<sub>2</sub>O hydrogen bonds are 0.6 and 0.5, respectively, for the hydrophobic pore, and 0.1 and 0.3, respectively for the hydrophilic pore. Hence,  $T\Delta S^{MD}$  is reasonably correlated to H<sub>2</sub>O molecule hydrogen bonds in the hydrophobic pore, but not in the hydrophilic pore. We find that  $T\Delta S^{MD}$  increases (becomes more positive) with the number of water-water hydrogen bonds and decreases (becomes more negative) with the number of water-adsorbate hydrogen bonds in the hydrophobic pore. In other words, in hydrophobic pores, H<sub>2</sub>O molecules that are hydrogen bonded to adsorbates have more negative  $T\Delta S^{MD}$  than H<sub>2</sub>O molecules that are hydrogen bonded to other H<sub>2</sub>O molecules. These results suggest that entropy of solvation is related to breaking and forming of hydrogen bonds between H<sub>2</sub>O molecules and adsorbates in hydrophobic pores.

#### 3.4.4 Adsorbate properties

Given the lack of clear quantitative relationship with  $T\Delta S^{MD}$  in hydrophilic pores, we investigated if adsorbate properties show correlation with  $T\Delta S^{MD}$ . A full list of properties that we considered is provided in Table S6. The adsorbate properties that give the largest correlation with  $T\Delta S^{MD}$  are SASA, dipole moment, and partial charge. These are plotted in Figure 7. We find R<sup>2</sup> values of 0.5, 0.2, and 0.3 for  $T\Delta S^{MD}$  with SASA, dipole moment, and partial charge, respectively, in hydrophobic pores and 0.4, 0.5, and 0.5 for  $T\Delta S^{MD}$  with SASA, dipole moment, and partial charge, respectively, in hydrophilic pores. Considering R<sup>2</sup> values equal to or greater than 0.4 as showing

potential correlation,  $T\Delta S^{MD}$  in hydrophobic pores is related to SASA, with larger adsorbates exhibiting more negative  $T\Delta S^{MD}$ . This agrees with the analysis above which indicates that adsorbates that displace more H<sub>2</sub>O molecules exhibit more negative  $T\Delta S^{MD}$  in hydrophobic pores. These two findings suggest that larger adsorbates exhibit more negative  $T\Delta S^{MD}$  in hydrophobic pores. Hence an entropic gain could be realized through a decomposition reaction in a hydrophobic pore, while entropic loss could be realized by an addition reaction in a hydrophobic pore.

In contrast,  $T\Delta S^{MD}$  in hydrophilic pores is related to adsorbate dipole moment and partial charge, with  $T\Delta S^{MD}$  decreasing (becoming more negative) as adsorbate dipole moment and partial charge increase. This suggests that the field created by the adsorbate contributes to  $T\Delta S^{MD}$  in hydrophilic pores, with stronger fields having a larger decrease on entropy. Interestingly, experiments have suggested an influence of polarity in hydrophilic zeolites, but this has been attributed to the pore<sup>39,75,76</sup>, whereas our results point to the polarity of the adsorbate. Based on this explanation, entropic gain should be realized in hydrophilic pores through conversion of a less polar species from a more polar one.

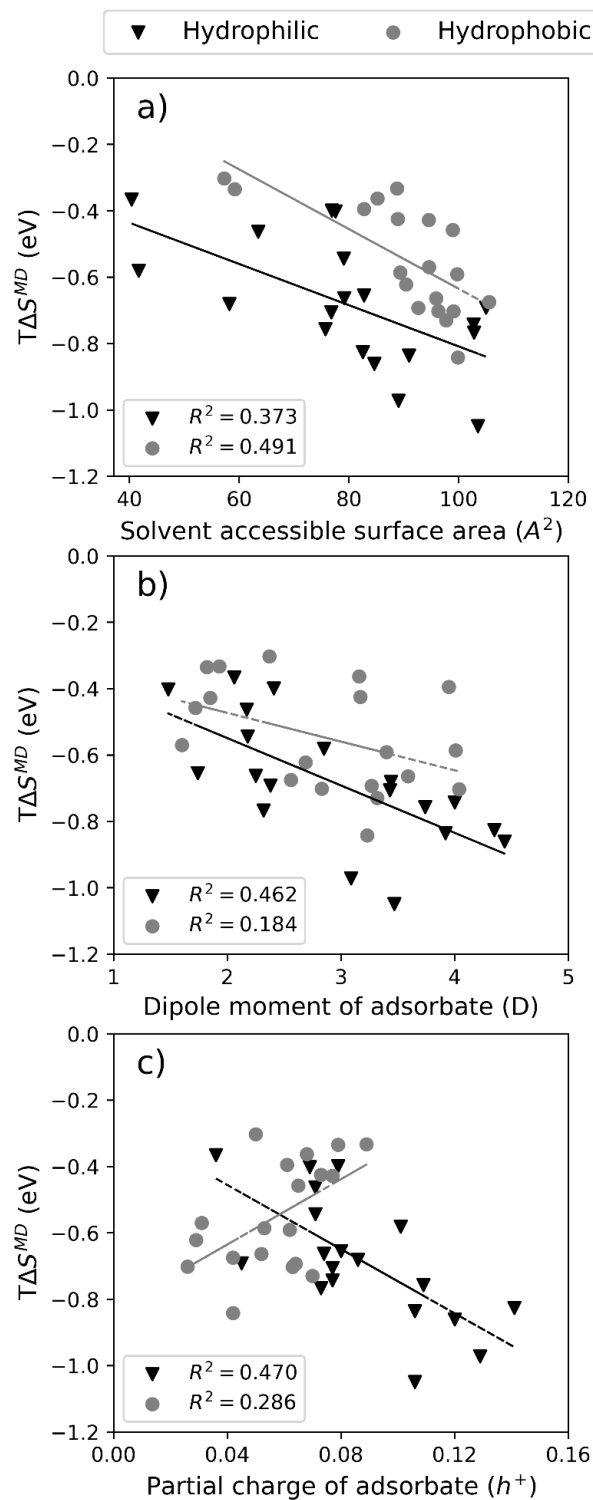


**Figure 7.** Temperature times entropy of solvation versus adsorbate solvent accessible surface area (a), adsorbate dipole moment (b), and adsorbate partial charge (c) for the hydrophilic (black triangles) and hydrophobic (gray circles) models. Lines are the least squares best fit lines and  $R^2$  values are the correlation coefficients.  $T = 300$  K.

#### 4. Discussion

Our simulations indicate significant differences in solvation energies, entropies, and free energies between our hydrophobic and hydrophilic pore models in hydrophilic Ti-FAU zeolite. Further, we find that solvation entropy (and hence free energy) has different origins, depending on whether the pore is hydrophobic or hydrophilic. In hydrophobic pores, a solvent structural property, specifically whether H<sub>2</sub>O molecules are hydrogen bonding with an adsorbate or other H<sub>2</sub>O molecules, influences entropy of solvation, whereas in hydrophilic pores, an adsorbate property, specifically related to adsorbate polarity, influences entropy of solvation. These results illustrate that solvation phenomena in confined systems are complicated, as well that it is unsurprising that experimental observations of different reactions in different zeolites using different solvents would result in seemingly conflicting behaviors. Our results show that solvation entropy (and hence free energy) depends on multiple phenomena. Further, we have only examined slight variations in zeolite active site. The influence of pore size, topology, and shape as well as contributions from reactant molecule mobility and the effect of cosolvents should be examined. These things are the topics of ongoing work.

#### 5. Conclusions

In this work, we studied the solvation thermodynamics of C<sub>1</sub>-C<sub>3</sub> oxygenates adsorbed to hydrophobic and hydrophilic pores within a hydrophilic zeolite, along with their relationships to solvent structure, solvent mobility, and adsorbate properties. Based on our results, which examine two different pores within one zeolite that has minimal unique adsorption sites, solvation thermodynamics vary significantly based on the pore environment and adsorbate, and solvation entropies (and hence solvation free energies) have different origins, depending on the pore

environment. There are multiple molecular level phenomena that contribute to solvation behavior in zeolites; the ones that are observed in catalysis experiments will depend on adsorbate, pore, and solvent properties, at least, as well as the particular rate determining features in the reaction.

## 6. Acknowledgments

This work was funded by the US Department of Energy under Award Number DE-SC0021170. Simulations were performed on the Ohio Supercomputer Center and the Palmetto Supercomputing Cluster at Clemson University. We thank Ricardo A. García Cárcamo (The Ohio State University and Clemson University), Dr. Jiarun Zhou (Clemson University), Prof. Sapna Sarupria (The University of Minnesota), and Prof. Nicholas A. Brunelli (The Ohio State University) for helpful discussions.

## References

1. Steinmann, S. N. & Michel, C. How to Gain Atomistic Insights on Reactions at the Water/Solid Interface? *ACS Catalysis* vol. 12 Preprint at <https://doi.org/10.1021/acscatal.2c00594> (2022).
2. Vega-Vila, J. C. & Gounder, R. Quantification of Intraporous Hydrophilic Binding Sites in Lewis Acid Zeolites and Consequences for Sugar Isomerization Catalysis. *ACS Catal* **10**, (2020).
3. Li, G., Wang, B. & Resasco, D. E. Solvent effects on catalytic reactions and related phenomena at liquid-solid interfaces. *Surface Science Reports* vol. 76 Preprint at <https://doi.org/10.1016/j.surfrep.2021.100541> (2021).
4. Varghese, J. J. & Mushrif, S. H. Origins of complex solvent effects on chemical reactivity and computational tools to investigate them: A review. *Reaction Chemistry and Engineering* vol. 4 Preprint at <https://doi.org/10.1039/c8re00226f> (2019).

5. Saleheen, M. & Heyden, A. Liquid-Phase Modeling in Heterogeneous Catalysis. *ACS Catalysis* vol. 8 Preprint at <https://doi.org/10.1021/acscatal.7b04367> (2018).
6. Zeets, M., Resasco, D. E. & Wang, B. Enhanced chemical activity and wettability at adjacent Brønsted acid sites in HZSM-5. *Catal Today* **312**, (2018).
7. Zeynep Ayla, E., Patel, D., Harris, A. & Flaherty, D. W. Identity of the metal oxide support controls outer sphere interactions that change rates and barriers for alkene epoxidations at isolated Ti atoms. *J Catal* **411**, (2022).
8. Li, G., Wang, B. & Resasco, D. E. Water-Mediated Heterogeneously Catalyzed Reactions. *ACS Catal* **10**, (2020).
9. Deluca, M., Janes, C. & Hibbitts, D. Contrasting Arene, Alkene, Diene, and Formaldehyde Hydrogenation in H-ZSM-5, H-SSZ-13, and H-SAPO-34 Frameworks during MTO. *ACS Catal* **10**, (2020).
10. Cordon, M. *et al.* Dominant Role of Entropy in Stabilizing Sugar Isomerization Transition States within Hydrophobic Zeolite Pores. *J Am Chem Soc* **140**, (2018).
11. Losch, P. *et al.* Modular Pd/Zeolite Composites Demonstrating the Key Role of Support Hydrophobic/Hydrophilic Character in Methane Catalytic Combustion. *ACS Catal* **9**, (2019).
12. Wang, L. *et al.* A significant enhancement of catalytic activities in oxidation with H<sub>2</sub>O<sub>2</sub> over the TS-1 zeolite by adjusting the catalyst wettability. *Chemical Communications* **50**, (2014).
13. Corma, A., Esteve, P. & Martínez, A. Solvent effects during the oxidation of olefins and alcohols with hydrogen peroxide on Ti-beta catalyst: The influence of the hydrophilicity-hydrophobicity of the zeolite. *J Catal* **161**, (1996).
14. Gould, N. S. *et al.* Understanding solvent effects on adsorption and protonation in porous catalysts. *Nat Commun* **11**, (2020).

15. Wang, C. H., Bai, P., Siepmann, J. I. & Clark, A. E. Deconstructing hydrogen-bond networks in confined nanoporous materials: Implications for alcohol-water separation. *Journal of Physical Chemistry C* **118**, (2014).
16. Hack, J. H. *et al.* Structural Characterization of Protonated Water Clusters Confined in HZSM-5 Zeolites. *J Am Chem Soc* **143**, (2021).
17. Bregante, D. T. *et al.* The shape of water in zeolites and its impact on epoxidation catalysis. *Nat Catal* **4**, 797–808 (2021).
18. Grifoni, E. *et al.* Confinement effects and acid strength in zeolites. *Nat Commun* **12**, (2021).
19. Potts, D. S., Bregante, D. T., Adams, J. S., Torres, C. & Flaherty, D. W. Influence of solvent structure and hydrogen bonding on catalysis at solid-liquid interfaces. *Chemical Society Reviews* vol. 50 12308–12337 Preprint at <https://doi.org/10.1039/d1cs00539a> (2021).
20. Bregante, D. T. *et al.* Cooperative effects between hydrophilic pores and solvents: Catalytic consequences of hydrogen bonding on alkene epoxidation in zeolites. *J Am Chem Soc* **141**, 7302–7319 (2019).
21. Hoffman, A. J. *et al.* Rigid Arrangements of Ionic Charge in Zeolite Frameworks Conferred by Specific Aluminum Distributions Preferentially Stabilize Alkanol Dehydration Transition States. *Angewandte Chemie - International Edition* **59**, 18686–18694 (2020).
22. Marsden, G. *et al.* Quantifying Effects of Active Site Proximity on Rates of Methanol Dehydration to Dimethyl Ether over Chabazite Zeolites through Microkinetic Modeling. *ACS Materials Au* **2**, (2022).
23. Chizallet, C., Bouchy, C., Larmier, K. & Pirngruber, G. Molecular Views on Mechanisms of Brønsted Acid-Catalyzed Reactions in Zeolites. *Chemical Reviews* vol. 123 Preprint at <https://doi.org/10.1021/acs.chemrev.2c00896> (2023).
24. Porter, A. J., McHugh, S. L., Omojola, T., Silverwood, I. P. & O'Malley, A. J. The effect of Si/Al ratio on local and nanoscale water diffusion in H-ZSM-5: A

- quasielastic neutron scattering and molecular dynamics simulation study. *Microporous and Mesoporous Materials* **348**, (2023).
25. Dusselier, M. & Davis, M. E. Small-Pore Zeolites: Synthesis and Catalysis. *Chemical Reviews* vol. 118 Preprint at <https://doi.org/10.1021/acs.chemrev.7b00738> (2018).
  26. Xu, H. & Wu, P. New progress in zeolite synthesis and catalysis. *National Science Review* vol. 9 Preprint at <https://doi.org/10.1093/nsr/nwac045> (2022).
  27. Polatoglu, I. & Cakicioglu-Ozkan, F. Aqueous interactions of zeolitic material in acidic and basic solutions. *Microporous and Mesoporous Materials* **132**, (2010).
  28. González-Rivera, J. *et al.* Heterogeneous catalytic reaction of microcrystalline cellulose in hydrothermal microwave-assisted decomposition: Effect of modified zeolite Beta. *Green Chemistry* **16**, (2014).
  29. Ennaert, T. *et al.* Potential and challenges of zeolite chemistry in the catalytic conversion of biomass. *Chemical Society Reviews* vol. 45 Preprint at <https://doi.org/10.1039/c5cs00859j> (2016).
  30. Liu, R., Dangwal, S., Shaik, I., Aichele, C. & Kim, S. J. Hydrophilicity-controlled MFI-type zeolite-coated mesh for oil/water separation. *Sep Purif Technol* **195**, (2018).
  31. Wang, C. *et al.* Regulation of hydrophilicity/hydrophobicity of aluminosilicate zeolites: a review. *Critical Reviews in Solid State and Materials Sciences* vol. 46 Preprint at <https://doi.org/10.1080/10408436.2020.1819198> (2021).
  32. Bukowski, B. C., Bates, J. S., Gounder, R. & Greeley, J. Defect-Mediated Ordering of Condensed Water Structures in Microporous Zeolites. *Angewandte Chemie* **131**, 16574–16578 (2019).
  33. Harris, J. W. *et al.* Molecular Structure and Confining Environment of Sn Sites in Single-Site Chabazite Zeolites. *Chemistry of Materials* **29**, (2017).
  34. Cordon, M. J. *et al.* Deactivation of Sn-Beta zeolites caused by structural transformation of hydrophobic to hydrophilic micropores during aqueous-phase glucose isomerization. *Catal Sci Technol* **9**, (2019).

35. Resasco, D. E., Crossley, S. P., Wang, B. & White, J. L. Interaction of water with zeolites: a review. *Catal Rev Sci Eng* **63**, (2021).
36. Balcom, H., Hoffman, A. J., Loch, H. & Hibbitts, D. Brønsted Acid Strength Does Not Change for Bulk and External Sites of MFI Except for Al Substitution Where Silanol Groups Form. *ACS Catal* **13**, (2023).
37. Zhang, L., Chen, K., Chen, B., White, J. L. & Resasco, D. E. Factors that Determine Zeolite Stability in Hot Liquid Water. *J Am Chem Soc* **137**, (2015).
38. Porter, A. J. & O'Malley, A. J. A Classical Molecular Dynamics Study on the Effect of Si/Al Ratio and Silanol Nest Defects on Water Diffusion in Zeolite HY. *Journal of Physical Chemistry C* **125**, 11567–11579 (2021).
39. Khechfe, A. A., Matha, T. B. M. & Román-Leshkov, Y. Solvent Polarity and Framework Hydrophobicity of Hf-BEA Zeolites Influence Aldol Addition Rates in Organic Media. *ACS Catal* **13**, (2023).
40. Di Iorio, J. R., Johnson, B. A. & Román-Leshkov, Y. Ordered hydrogen-bonded alcohol networks confined in lewis acid zeolites accelerate transfer hydrogenation turnover rates. *J Am Chem Soc* **142**, (2020).
41. Yang, G., Pidko, E. A. & Hensen, E. J. M. The mechanism of glucose isomerization to fructose over Sn-BEA zeolite: a periodic density functional theory study. *ChemSusChem* **6**, 1688–1696 (2013).
42. Potts, D. S. *et al.* Effect of Interactions between Alkyl Chains and Solvent Structures on Lewis Acid Catalyzed Epoxidations. *ACS Catal* **12**, (2022).
43. Tan, J. Z., Bregante, D. T., Torres, C. & Flaherty, D. W. Transition state stabilization depends on solvent identity, pore size, and hydrophilicity for epoxidations in zeolites. *J Catal* **405**, (2022).
44. Bates, J. S., Bukowski, B. C., Greeley, J. & Gounder, R. Structure and solvation of confined water and water-ethanol clusters within microporous Brønsted acids and their effects on ethanol dehydration catalysis. *Chem Sci* **11**, (2020).

45. Li, G., Wang, B., Kobayashi, T., Pruski, M. & Resasco, D. E. Optimizing the surface distribution of acid sites for cooperative catalysis in condensation reactions promoted by water. *Chem Catalysis* **1**, (2021).
46. Grosso-Giordano, N. A. *et al.* Dynamic Reorganization and Confinement of TiIV Active Sites Controls Olefin Epoxidation Catalysis on Two-Dimensional Zeotypes. *J Am Chem Soc* **141**, (2019).
47. Vener, M. V., Rozanska, X. & Sauer, J. Protonation of water clusters in the cavities of acidic zeolites: (H<sub>2</sub>O)<sub>n</sub>-H-chabazite, n = 1-4. *Physical Chemistry Chemical Physics* **11**, (2009).
48. Li, Y.-P., Head-Gordon, M. & Bell, A. T. Analysis of the reaction mechanism and catalytic activity of metal-substituted beta zeolite for the isomerization of glucose to fructose. *ACS Catal* **4**, 1537–1545 (2014).
49. Zhang, X., DeFever, R. S., Sarupria, S. & Getman, R. B. Free Energies of Catalytic Species Adsorbed to Pt(111) Surfaces under Liquid Solvent Calculated Using Classical and Quantum Approaches. *J Chem Inf Model* **59**, 2190–2198 (2019).
50. Baerlocher, C. Database of zeolite structures. [http://www. iza-structure.org/databases/](http://www.iza-structure.org/databases/) (2008).
51. Garcia Carcamo, R. A. *et al.* Differences in solvation thermodynamics of oxygenates at Pt/Al<sub>2</sub>O<sub>3</sub> perimeter versus Pt(111) terrace sites. *iScience* **26**, (2023).
52. Estejab, A., Cárcamo, R. A. G. & Getman, R. B. Influence of an electrified interface on the entropy and energy of solvation of methanol oxidation intermediates on platinum (111) under explicit solvation. *Physical Chemistry Chemical Physics* **24**, 4251–4261 (2022).
53. Zhang, X., DeFever, R. S., Sarupria, S. & Getman, R. B. Free energies of catalytic species adsorbed to pt (111) surfaces under liquid solvent calculated using classical and quantum approaches. *J Chem Inf Model* **59**, 2190–2198 (2019).

54. Thompson, A. P. *et al.* LAMMPS-a flexible simulation tool for particle-based materials modeling at the atomic, meso, and continuum scales. *Comput Phys Commun* **271**, 108171 (2022).
55. Jorgensen, W. L. & Jenson, C. Temperature dependence of TIP3P, SPC, and TIP4P water from NPT Monte Carlo simulations: Seeking temperatures of maximum density. *J Comput Chem* **19**, (1998).
56. Saiz, L., Guàrdia, E. & Padró, J. À. Dielectric properties of liquid ethanol. A computer simulation study. *Journal of Chemical Physics* **113**, (2000).
57. Nandi, N., Bhattacharyya, K. & Bagchi, B. Dielectric relaxation and solvation dynamics of water in complex chemical and biological systems. *Chem Rev* **100**, (2000).
58. MacKerell Jr, A. D. *et al.* All-atom empirical potential for molecular modeling and dynamics studies of proteins. *J Phys Chem B* **102**, 3586–3616 (1998).
59. Bai, P., Tsapatsis, M. & Siepmann, J. I. TraPPE-zeo: Transferable potentials for phase equilibria force field for all-silica zeolites. *The Journal of Physical Chemistry C* **117**, 24375–24387 (2013).
60. Jorgensen, W. L., Maxwell, D. S. & Tirado-Rives, J. Development and Testing of the OPLS All-Atom Force Field on Conformational Energetics and Properties of Organic Liquids. *J Am Chem Soc* **118**, 11225–11236 (1996).
61. Brandt, E. G. & Lyubartsev, A. P. Systematic optimization of a force field for classical simulations of TiO<sub>2</sub>–water interfaces. *The Journal of Physical Chemistry C* **119**, 18110–18125 (2015).
62. Matsui, M. & Akaogi, M. Molecular dynamics simulation of the structural and physical properties of the four polymorphs of tio<sub>2</sub>. *Mol Simul* **6**, (1991).
63. Mezei, M. The finite difference thermodynamic integration, tested on calculating the hydration free energy difference between acetone and dimethylamine in water. *J Chem Phys* **86**, (1986).

64. Shirts, M. R. & Pande, V. S. Solvation free energies of amino acid side chain analogs for common molecular mechanics water models. *Journal of Chemical Physics* **122**, (2005).
65. Kühne, T. D. *et al.* CP2K: An electronic structure and molecular dynamics software package-Quickstep: Efficient and accurate electronic structure calculations. *J Chem Phys* **152**, 194103 (2020).
66. Grimme, S., Ehrlich, S. & Goerigk, L. Effect of the damping function in dispersion corrected density functional theory. *J Comput Chem* **32**, 1456–1465 (2011).
67. Manz, T. A. & Limas, N. G. Introducing DDEC6 atomic population analysis: part 1. Charge partitioning theory and methodology. *RSC Adv* **6**, 47771–47801 (2016).
68. Schrödinger, L. L. C. & DeLano, W. PyMOL. Preprint at <http://www.pymol.org/pymol>.
69. Piccini, G., Alessio, M. & Sauer, J. Ab initio study of methanol and ethanol adsorption on Brønsted sites in zeolite H-MFI. *Physical Chemistry Chemical Physics* **20**, (2018).
70. Van Der Mynsbrugge, J., Hemelsoet, K., Vandichel, M., Waroquier, M. & Van Speybroeck, V. Efficient approach for the computational study of alcohol and nitrile adsorption in H-ZSM-5. *Journal of Physical Chemistry C* **116**, (2012).
71. Bukowski, B. C., Bates, J. S., Gounder, R. & Greeley, J. First principles, microkinetic, and experimental analysis of Lewis acid site speciation during ethanol dehydration on Sn-Beta zeolites. *J Catal* **365**, (2018).
72. Shetty, S., Kulkarni, B. S., Kanhere, D. G., Goursot, A. & Pal, S. A comparative study of structural, acidic and hydrophilic properties of Sn - BEA with Ti - BEA using periodic density functional theory. *Journal of Physical Chemistry B* **112**, (2008).
73. Zhu, H. *et al.* Investigation of dielectric constants of water in a nano-confined pore. *RSC Adv* **10**, (2020).

74. Choudhury, N. & Pettitt, B. M. Dynamics of water trapped between hydrophobic solutes. *Journal of Physical Chemistry B* **109**, (2005).
75. Gounder, R. & Davis, M. E. Beyond shape selective catalysis with zeolites: Hydrophobic void spaces in zeolites enable catalysis in liquid water. *AIChE Journal* **59**, (2013).
76. Zhang, Z., Berdugo-Díaz, C. E., Bregante, D. T., Zhang, H. & Flaherty, D. W. Aldol Condensation and Esterification over Ti-Substituted \*BEA Zeolite: Mechanisms and Effects of Pore Hydrophobicity. *ACS Catal* **12**, (2022).
77. van der Graaff, W. N. P. *et al.* Competitive Adsorption of Substrate and Solvent in Sn-Beta Zeolite During Sugar Isomerization. *ChemSusChem* **9**, (2016).